Koc. J. Sci. Eng., 8(1): (2025) 38-51 https://doi.org/10.34088/kojose.1556617

Kocaeli University

Kocaeli Journal of Science and Engineering

http://dergipark.org.tr/kojose

Quantitative Assessment of Image Reconstruction Algorithms in Electrical Impedance Tomography

Ibrahim OZ [1, *]

[1] *Earth and Space Science Institution, Eskisehir Technical University, Eskişehir, Türkiye,* ***ORCID:*** *0000-0003-4593-917X*

Article Info

Research paper

Received *: September 26, 2024*
Accepted *: December 21, 2024*

Keywords

Electrical Impedance Tomography
image reconstruction
inverse problem
delta conductivity
Jacobian matrix
Finite Element Method

Abstract

Electrical Impedance Tomography (EIT) is a noninvasive imaging technique used to estimate the internal conductivity distribution of a region that is either unknown or inaccessible. This is achieved by applying electrical currents to the region and measuring the resulting boundary voltages. The forward problem in EIT is typically solved using the Finite Element Method (FEM), and regularization techniques are employed to stabilize the ill-posed inverse problem during image reconstruction. This study evaluated the performance of two widely used image reconstruction algorithms: the delta conductivity method and the Jacobian (JAC)-based method. Both algorithms were tested on seven phantom images with varying levels of complexity to assess their effectiveness in different scenarios. The average Peak Signal-to-Noise Ratio (PSNR) and Mean Structural Similarity Index (MSSIM) were 35.71 dB and 0.93, respectively, indicating high reconstruction quality. However, the complexity of the images, such as intricate textures or multiple inclusions, resulted in reduced reconstruction accuracy. Although, both the delta conductivity and JAC methods proved effective in EIT image reconstruction, the JAC method shows superior performance in more challenging cases.

1. Introduction

Electrical impedance tomography (EIT) is a non-destructive imaging technique used to estimate the electrical conductivity of an unknown or inaccessible region. It is widely employed in applications where direct conductivity measurement within a domain is impractical or impossible. Instead, boundary measurements of electrical potentials are utilized, and the internal conductivity distribution is inferred through mathematical inversion techniques. This approach is particularly beneficial in medical imaging [1, 2].

One of the fundamental challenges in EIT is that the inversion problem is typically ill-posed, a concept first formalized by Jacques Hadamard. An ill-posed problem, as opposed to a well-posed one, fails to satisfy one or more of the following conditions: 1) the existence of a solution, 2) the uniqueness of the solution, and 3) the stability of the solution to small perturbations in the input data. The ill-posed nature of the EIT inverse problem arises because there are generally more unknown conductivity parameters than available measurements. Consequently, small errors in the data can lead to large deviations in the estimated conductivity, requiring careful regularization and robust computational methods for reliable solutions [3, 4].

Various reconstruction algorithms have been developed for EIT in the literature. Due to the highly ill-posed nature of EIT, achieving noise-robust reconstructions requires regularization techniques in nearly all methods. Traditional imaging approaches typically incorporate prior information to stabilize the inversion process, achieved through various regularization techniques [5-7]. These methods generally involve discrete approximations of the forward model, followed by solving a finite-dimensional minimization problem using iterative algorithms. Among these, gradient-based methods are commonly employed due to their ability to handle large-scale problems efficiently.

A linearized model is often employed to simplify the inversion process in such iterative methods. Linearization helps reduce the problem's computational complexity but

---

[*] Corresponding Author: ibrahimoz@gazi.edu.tr

introduces challenges in achieving high-resolution reconstructions, especially when noise is present in the data. Regularization plays a critical role here by ensuring the inversion remains stable, even under noisy conditions. Popular regularization techniques include Tikhonov regularization, total variation regularization, and L2/L1 norms. These techniques allow the algorithms to fit the data in a balanced way and maintain smoothness or sparsity in the reconstructed images.

In contrast to iterative approaches, several direct algorithms have been developed, offering faster computation by bypassing the need for forward simulations. Examples of these methods include the factorization method, the D-bar method, Calderón's method, and the direct sampling method [8-11]. These methods rely on different mathematical frameworks and do not require iterative refinement, making them more computationally efficient.

While iterative reconstruction methods with regularization offer improved accuracy and robustness in noisy conditions, they are computationally expensive. On the other hand, direct algorithms like Calderón's method provide faster results but with lower resolution, highlighting the trade-off between computational efficiency and reconstruction quality.

In typical EIT experiments, a set of electrodes is distributed along the boundary of the region of interest. In geophysical applications, these electrodes are often placed on the earth's surface, whereas in medical contexts, they are positioned around the body. The electrodes serve a dual purpose: they inject electrical current into the domain and measure the resulting voltages at various points on the boundary. Multiple current injection patterns are employed to obtain sufficient data for reconstructing the internal conductivity distribution. L distinct injection patterns are usually performed for a system comprising L electrodes, each resulting in L voltage measurements. This process yields a total of $L \times L$ measurements, which are used in the inversion process to estimate the conductivity distribution [12, 13]

To model and solve the forward problem in EIT, the Finite Element Method (FEM) is commonly used. Given the conductivity and the applied current, the forward problem involves computing the voltage distribution on the domain's boundary. In implementing the forward problem, we initially adopted a simplified electrode model, where current is assumed to flow into and out of the imaging domain, Ω, through specific boundary nodes that serve as electrodes. Although this approach simplifies the problem, it does not consider all practical considerations. A more accurate representation is provided by the Complete Electrode Model (CEM), which incorporates the finite size and impedance of the electrodes [14].

EIDORS (Electrical Impedance Tomography and Diffuse Optical Reconstruction Software) is an open-source software suite for research and development in EIT and related imaging techniques. EIDORS provides a comprehensive platform for simulating, reconstructing, and visualizing EIT data, making it a valuable tool for academic and industrial applications. The software supports a range of functionalities, including forward and inverse problem solving, mesh generation, and electrode modeling, which are crucial for accurate image reconstruction in EIT [15].

By offering various reconstruction algorithms, including direct methods and regularization techniques, EIDORS enables users to implement and compare different approaches for solving the ill-posed nature of the EIT inverse problem. EIDORS also supports multi-frequency EIT, allowing researchers to investigate the frequency-dependent behavior of materials. Its flexibility and extensive documentation make it widely used in medical imaging, geophysical explorations, and industrial non-destructive testing. Using EIDORS, researchers can efficiently evaluate the performance of various algorithms and improve the accuracy of conductivity reconstructions in EIT.

2. Modeling and Image Reconstruction

This study uses the following steps for modeling and image reconstruction. Figure 1 presents the flowchart illustrating the key steps: input data preparation, implementation of the delta conductivity algorithm, application of the Jacobian (JAC) algorithm, image reconstruction processes, result comparisons, and performance evaluation.

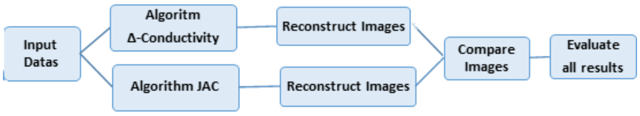

Figure 1. A flowchart outlining the steps of the study.

In EIT, the forward problem involves computing the voltage distribution at the domain's boundary, given the internal conductivity distribution and the applied current. The governing equation for the forward problem in EIT is derived from Ohm's Law and the conservation of current [16, 17].

The continuity equation for the electric potential can describe the mathematical formulation of the forward problem;

$$\nabla \cdot (\sigma(x)\nabla u(x)) = 0, \quad \text{in} \quad \Omega \qquad (1)$$

where:

- $\sigma(x)$ is the electrical conductivity at position x inside the domain Ω,
- $u(x)$ is the electric potential at position x,
- $\nabla\cdot$ represents the divergence operator, and
- $\nabla u(x)$ is the gradient of the electric potential, which gives the electric field.

By solving this forward problem, the voltage distribution on the boundary is obtained, and this information is later used in the inverse problem to estimate the internal conductivity distribution.

2.1. Boundary Conditions

The boundary conditions for this problem are defined on the boundary $\partial\Omega$, where electrodes are placed to inject current and measure voltage. For the simplified electrode model, we assume that the current flows through boundary nodes, which serve as electrodes [18, 19]. The total current injected through each electrode satisfies:

$$\int_{e_k} \sigma \frac{\partial U}{\partial n} ds = I_l \text{ for } k_1 = 1,2,\ldots\ldots, L \qquad (2)$$

where:

- e_k is the region on the boundary where the
- kth electrode is located,
- $\partial u/\partial n$ represents the normal derivative of the potential at the boundary (i.e., the current density),
- I_k is the current injected through the k-th electrode,
- L is the number of electrodes

Grounding or reference electrode condition: To resolve the potential uniquely, we impose a reference potential condition, usually by grounding one of the electrodes on a reference electrode or part of $\partial\Omega$.

2.2. Finite Element Method (FEM) Discretization

In practical EIT simulations, the FEM is used to solve the above system numerically. The domain Ω is discretized into elements, and the continuous problem is converted into a discrete system. Using FEM, the problem is transformed into a linear system and can be expressed:

$$K(\sigma)U = F \qquad (3)$$

Where;

- ***K(σ)*** is stiffness matrix that depends on the conductivity distribution of $\sigma(x)$.
- ***U*** is the vector of nodal potentials.
- ***F*** is the vector of nodal current injections corresponding to the boundary conditions.

2.3. Image Reconstruction (Inverse Problem)

In EIT, the image reconstruction process refers to estimating the internal conductivity distribution $\sigma(x)$ within a domain from boundary voltage measurements. The inverse problem is also called image reconstruction, which can be described as;

$$\sigma = F\,(\cdot) \cdot \mathrm{U} \qquad (4)$$

where $F\,(\cdot)$ denotes the mapping relation between the boundary-measured voltages U and the interior conductivity distribution σ.

Various methods can be employed to regularize the inversion, including perturbation-based reconstruction using changes in conductivity (often called Δ conductivity) and JAC-based approaches [20-22].

2.3.1. Image Reconstruction Using Delta Conductivity (Perturbation-Based Method)

The delta conductivity method involves updating the conductivity distribution $\sigma(x)$ iteratively, based on small perturbations or changes in the boundary measurements. This technique is used when the initial guess for the conductivity distribution is close to the true distribution, and a minor correction is required to improve the estimate.

Algorithm Δ-Conductivity based Image Construction

```
1. Initialization:
    • Set the initial guess for the conductivity distribution $\sigma \leftarrow \sigma_0$
    • Define the forward model $F(\sigma)$, representing the relation between the conductivity $\sigma$ and the measured /simulated voltage data.
    • Define a regularization matrix $R$ (e.g., identity matrix on prior knowledge).
2. Forward Problem Simulation:
    • Compute the predicted voltage data based on the current estimate of conductivity:
          $V_{pred} \leftarrow F\,(\sigma)$
    • Calculate the difference between the measured and predicted voltages:
          $\Delta V \leftarrow V_{meas} - V_{pred}$
3. Compute Δ-Conductivity Sensitivity ($\Delta\sigma$):
    • Compute the sensitivity of the voltage data to change in conductivity matrix $\Delta(\sigma)$, which models changes in the conductivity needed to reduce the difference in voltage:
          $\Delta\sigma = (J^T J + \lambda\,\mathrm{R})^{-1} J^T\,\Delta V$
```

```
4. Update Conductivity Distribution:
    • Update the conductivity distribution by adding the calculated delta conductivity:
          $\sigma \leftarrow \sigma + \Delta$:
5. Check for Convergence:
    • Compute the norm of the delta conductivity
          $||\Delta\sigma|| < \epsilon$
    • If the norm of the update $||\Delta\sigma||$ is smaller than the defined tolerance $\epsilon$, terminate the algorithm.
6. Repeat Iteration:
    • If convergence is not achieved, return to Step 2 and repeat the process until the reconstruction stabilizes.
```

The delta-conductivity method iteratively updates the conductivity distribution by calculating changes based on the difference between the measured and predicted voltages. In each iteration, the change in conductivity ($\Delta\sigma$) is computed to minimize this voltage discrepancy. Regularization is critical in stabilizing the reconstruction process, particularly in noisy conditions, by preventing overfitting to the data. The algorithm continues to iterate, refining the conductivity estimates until the updates become sufficiently small, ensuring convergence to an accurate solution while maintaining robustness against noise.

2.3.2. Image Reconstruction Using JAC Method

The Jacobian matrix J plays a critical role in reconstructing the conductivity distribution in EIT. It represents the sensitivity of boundary voltage measurements to small changes in the conductivity distribution. The Jacobian is typically computed as part of the forward problem solution using FEM.

Algorithm JAC-based Image Construction

```
1. Initialization:
    • Set the initial guess for the conductivity distribution $\sigma \leftarrow \sigma_0$
    • Define the forward model $F(\sigma)$, representing the relation between the conductivity $\sigma$ and the measured voltage data.
    • Define a regularization matrix $R$(e.g., identity matrix for Tikhonov regularization).
2. Forward Problem Simulation:
    • Compute the predicted voltage data based on the current estimate of conductivity:
          $V_{pred} \leftarrow F(\sigma)$
    • Compute the difference between the measured and predicted voltages:
          $\Delta V \leftarrow V_{meas} - V_{pred}$
3. Jacobian Calculation:
    • Compute the Jacobian matrix $J(\sigma)$, which represents the sensitivity of the voltage data with respect to changes in the conductivity:
          $J \leftarrow \partial F(\sigma) / \partial \sigma$
4. Solve for Conductivity Update:
    • Use the Jacobian and a regularization method to compute the conductivity update $\Delta\sigma$:
          $\Delta\sigma = ( J^T J + \lambda R )^{-1} J^T \Delta V$
    • Update the conductivity estimate:
          $\sigma = \sigma + \Delta\sigma$
5. Check for Convergence:
    • Calculate the norm of the conductivity update $||\Delta\sigma||$:
          $||\Delta\sigma|| < \epsilon$
    • If the change in conductivity is smaller than the tolerance $\epsilon$, terminate the algorithm.
6. Repeat Iteration:
    • If convergence is not achieved, return to Step 2 and repeat the process until the solution converges.
```

The Jacobian-based image reconstruction algorithm in EIT begins with inputting measured voltage data V_{meas} from boundary electrodes, an initial guess for the conductivity distribution F(σ) that simulates the voltage data based on a given conductivity distribution. The conductivity update is solved by minimizing the error in voltage data. This process repeats until the change in conductivity falls below the convergence threshold, at which point the reconstructed conductivity distribution is returned as the output.

2.4. Evaluation Metrics

In EIT, several metrics are commonly employed to assess the quality of the reconstructed image, including the image correlation coefficient (CC) and the relative error (RE). The RE quantifies the difference in conductivity between the reconstructed and original images. At the same time, the CC measures the correlation between them, providing insight into how closely the reconstructed image matches the original [23, 35].

In this study, two prominent image quality metrics, Peak Signal-to-Noise Ratio (PSNR) and Mean Structural Similarity Index Measure (MSSIM), were employed to assess image reconstruction performance in EIT. These metrics provide complementary insights into the fidelity and structural integrity of the reconstructed images.

PSNR has been used to evaluate the quality of the reconstructed image. The PSNR is a metric that quantifies the peak error between the reconstructed and original images in decibels (dB) [24-27]. It is particularly useful for data represented in terms of bits per sample or bits per pixel. A higher PSNR value indicates better image quality, with a PSNR above 40 dB suggesting that the reconstructed image is nearly indistinguishable from the original. The following equation defines the PSNR:

$$\mathrm{PSNR} = 10\log_{10}\left(\frac{\max^2}{\mathrm{MSE}}\right) \quad (5)$$

max: color depth. For 8 bits max=2^8-1=255, and mean square error can be calculated with Equation 6;

$$\mathrm{MSE} = \frac{1}{mn}\sum_{i=0}^{m=1}\sum_{j=0}^{n=1}|X(i,j) - X_c(i.j)|^2 \quad (6)$$

Where, M and N represent the size of the image, X represents the given input image and X_c represents the reconstructed image.

To evaluate the quality of the reconstructed images, we employ two metrics: the Relative Image Error (RIE) to quantify the accuracy of the estimated conductivity values and the Mean Structural Similarity Index (MSSIM) to assess the structural similarity between the ground truth and the reconstructed images. The RIE is defined as follows:

$$RIE = \frac{\|D_e - D_r\|}{\|D_r\|} \quad (7)$$

where D_e represents the reconstructed image, while D_r denotes the ground truth image. The subscripts e and r correspond to the estimated EIT image and the ground truth image, respectively.

While PSNR focuses on pixel-wise differences, the Mean Structural Similarity Index Measure (MSSIM) assesses image quality by comparing the structural information between the original and reconstructed images. MSSIM evaluates luminance, contrast, and structural similarity, offering a more perceptually meaningful assessment of image quality [28,29]. The MSSIM is defined as:

$$\mathrm{MSSIM} = \frac{1}{N}\sum\frac{(2\mu_e\mu_r + C_1)(2\varphi_{e,r} + C_2)}{(\mu_e^2\mu_r^2 + C_1)(\varphi_e^2 + \varphi_r^2 + C_2)} \quad (8)$$

where the summation is over all pixels of the EIT image. μ_e and μ_r are the local means. φe and φ_r are local standard deviations. φ_{er} denotes the cross-covariance between the estimated EIT image and the ground truth image. C1 and C2 represent constants.

By utilizing both PSNR and MSSIM, we comprehensively evaluate the image reconstruction quality in EIT. PSNR quantifies the overall error magnitude, while MSSIM provides insight into how well the reconstruction preserves structural information. Combining these two metrics allows for a more robust assessment, ensuring that the reconstructed image minimizes pixel-wise errors and retains the original's important structural features.

3. Dataset and Simulation Setup

In this study, a circular phantom with a radius of 1 cm was employed as the domain for EIT simulations. A total of 16 evenly spaced electrodes were placed around the boundary of the phantom to inject current and measure voltages. The opposite current injection technique was adopted for data collection, which involves injecting current through one electrode and receiving it from another electrode positioned directly opposite on the boundary.

Specifically, in this configuration, current is first injected from the first electrode and received at the ninth electrode (the opposite electrode on the circular boundary). The corresponding voltage differences between all other electrode pairs are then measured, capturing the potential distribution across the domain. After this initial measurement, the current injection and reception points are shifted to the next electrode pair and repeated. The electrodes are systematically shifted around the boundary, ensuring comprehensive coverage of voltage data for all possible electrode configurations [30-32].

This method is advantageous because it provides a wide range of voltage measurements for a given current pattern, enhancing the sensitivity of the reconstruction algorithm to variations in conductivity within the phantom. Figure 2 illustrates the current injection pattern and the voltage measurement scheme used in the experiment. This opposite current injection method generates a detailed and robust dataset, which is critical for accurate image reconstruction in EIT.

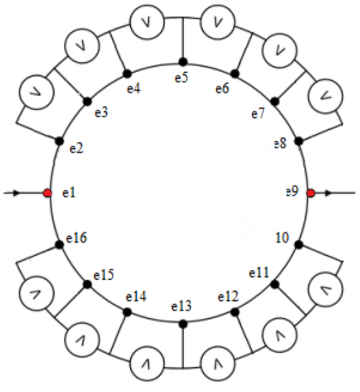

Figure 2. Schematic diagram of a 16-electrode phantom, illustrating opposite current injection and the measurement / simulation of voltage values.

FEM was applied to solve the problems in EIT, the domain was discretized into a mesh consisting of 664 nodes. These nodes form the vertices of the elements that define the mesh structure, which, in this case, results in a total of 1244 elements, as illustrated in Figure 3. Each element, typically triangular in shape for 2D FEM analysis, serves as a small subregion where the conductivity and potential distribution are approximated.

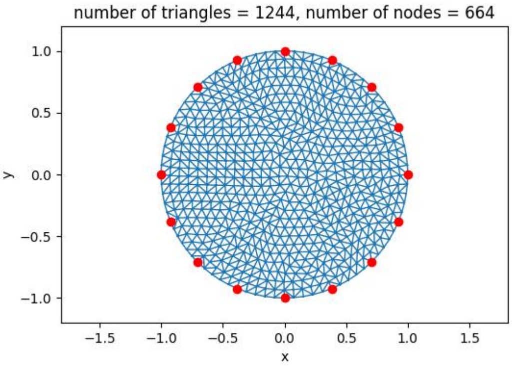

Figure 3. The images are divided into 1,244 triangles (meshes/elements) and contain 664 nodes.

This discretization allows for a detailed numerical representation of the continuous conductivity field within the phantom. The FEM framework uses these nodes and elements to approximate the solution of partial differential equations governing the electrical potential distribution. By dividing the domain into small, manageable elements, FEM provides a robust method for solving complex geometries and varying conductivity distributions, ensuring accurate simulation of current flow and voltage measurements. Figure 3 shows the meshing structure used in this study, demonstrating how the computational domain is subdivided into smaller elements for analysis. This discretization level balances computational efficiency and accuracy, which is crucial for capturing the detailed conductivity variations required for precise image reconstruction.

3.1. Test Images

In this study, a circular domain with a radius of 1 cm and a homogeneous conductivity σ=1 S/cm was selected as the base model for EIT simulations.

Figure 4 illustrates the theoretical geometric shapes of the test images used in EIT simulations. These shapes represent various conductivity inclusions introduced into the phantom, designed to evaluate the performance of the image reconstruction algorithms. Each test image consists of a specific configuration of regions with varying conductivity values inserted into a homogeneous background. The geometric shapes include circular inclusions, single and multiple holes, and arrangements of inclusions at different positions within the domain.

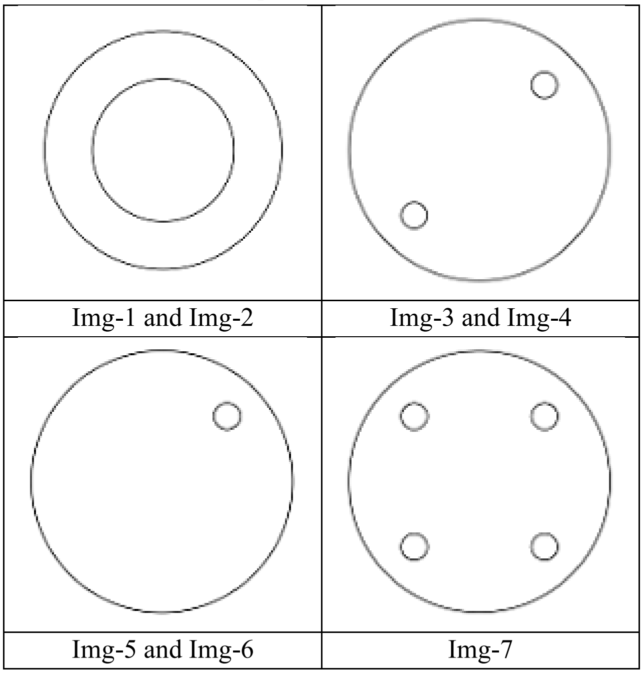

Img-1 and Img-2

Img-3 and Img-4

Img-5 and Img-6

Img-7

Figure 4. Theoretical geometric shapes of the test images.

Several variations of test phantoms were generated to assess the performance of the image reconstruction algorithms. These phantoms were designed by inserting regions with different conductivities and geometries into the base model.

Single Circular Inclusion: A circular inclusion with a radius r= 0.6 cm was introduced at the center of the domain. Two different conductivities were assigned to this inclusion: σ =5 S/cm, representing a highly conductive material (Img-1) and σ = 0.1 S/cm, representing a poorly conductive material (Img-2).

Single Hole in the Upper Corner: A single inclusion was placed at the top corner of the domain, with conductivities: σ =5 S/cm (Img-3) and σ =0.1 S/cm (Img-4).

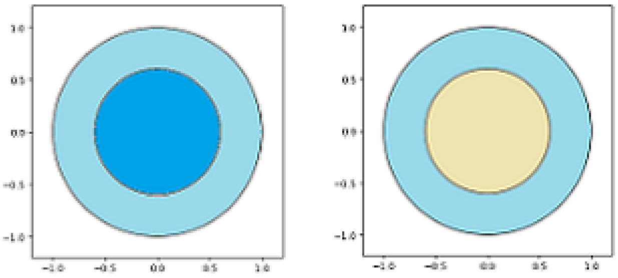

Img-1 Img-2

Figure 5. Theoretical shapes of test images colored according to conductivity

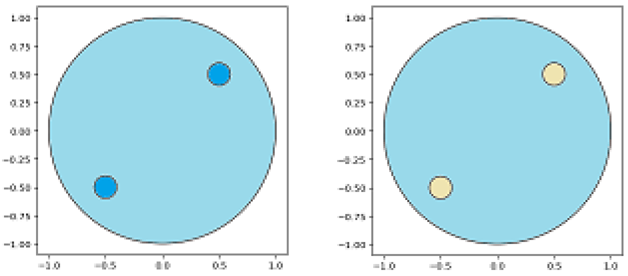

Img-3 Img-4

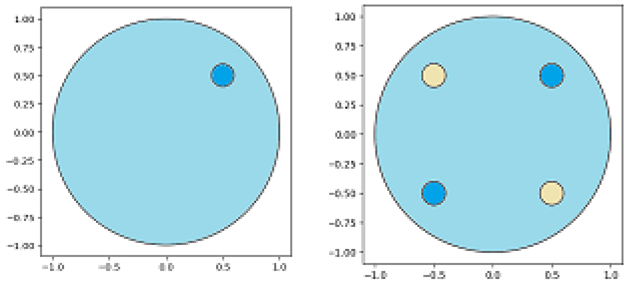

Img-5 Img-7

Figure 5. (Cont.) Theoretical shapes of test images colored according to conductivity

Double Holes (Diagonal Configuration): Two inclusions were positioned, one in the upper right corner and the other in the lower left corner. These inclusions were assigned the following conductivities: Upper right corner: σ = 5 S/cm (Img-5) and Lower left corner: σ = 0.1 S/cm (Img-6).

Four Holes (Quadrant Configuration): Four inclusions were inserted into the domain, one in each quadrant. The conductivities were distributed as follows: Upper right and lower left: σ = 5 S/cm and Upper left and lower right: σ = 0.1S/cm (Img-7).

Figure 5 presents the theoretical shapes of the test images used in this study, with each image color-coded according to its assigned conductivity values. These test images represent different conductivity distributions, where regions with varying conductivity levels are embedded within a homogeneous background. The color scheme highlights the conductivity contrasts, with high-conductivity regions in dark blue and low-conductivity regions in yellow, providing a clear visual representation of the spatial variations in electrical properties.

In this study, the theoretical images were carefully designed to serve as benchmarks for evaluating the performance of the image reconstruction algorithms. Each test image incorporates specific geometric shapes, including circular inclusions, single holes, and multiple holes, strategically positioned within the domain to simulate diverse conductivity patterns. The conductivity values of these regions were deliberately varied to create distinct contrasts with the homogeneous background, posing challenges to the reconstruction process. These images were also selected to model the conductivity variations typically observed in human tissues, such as differences between lesions and other biological structures, thereby enhancing the practical relevance of the evaluation. This approach ensures a difficult assessment of the algorithms' ability to resolve complex and realistic conductivity distributions for applications in biomedical imaging.

A Python-based code was developed to solve the forward problem, EIT. The forward problem was addressed using FEM, where the domain is discretized into a mesh of nodes and elements to simulate voltage distributions for given conductivity values [33].

The code was also designed to implement two image reconstruction algorithms: the delta conductivity update method and the JAC method. These methods iteratively update the conductivity distribution based on the difference between measured and simulated voltages, and regularization techniques were applied to ensure stable reconstructions. In addition, the code calculates key performance metrics, including PSNR, MSE, and MSSIM, to quantitatively assess the quality of the reconstructed images. This Python-based solution provides a flexible, efficient platform for testing and evaluating various EIT algorithms and their accuracy in image reconstruction.

4. Results

In this study, seven distinct test images, labeled from Img-1 to Img-7, were analyzed to evaluate the performance of the image reconstruction algorithms in EIT. Each of these images represents a unique configuration of conductivity inclusions within the phantom, designed to test the system's ability to detect and accurately reconstruct variations in conductivity. The forward problem, which involves simulating the voltage measurements based on the known conductivity distribution, was solved for each test image using FEM.

FEM was employed to discretize the computational domain into a mesh, allowing for an accurate numerical solution of the partial differential equations governing the current and voltage distributions within the domain. This step is critical for generating the simulated voltage data, which serves as the input for the inverse problem of reconstructing the conductivity distribution. The application of FEM ensured that the complex geometries and conductivity contrasts present in the test images were captured with high precision, providing a reliable basis for the subsequent image reconstruction process.

Figure 6 presents four selected test images from the total of seven analyzed in this study, illustrating the distribution of equipotential lines calculated by solving the forward problem. Each test image showcases how the equipotential lines adapt in response to the size and conductivity properties of the inclusions embedded within the phantom.

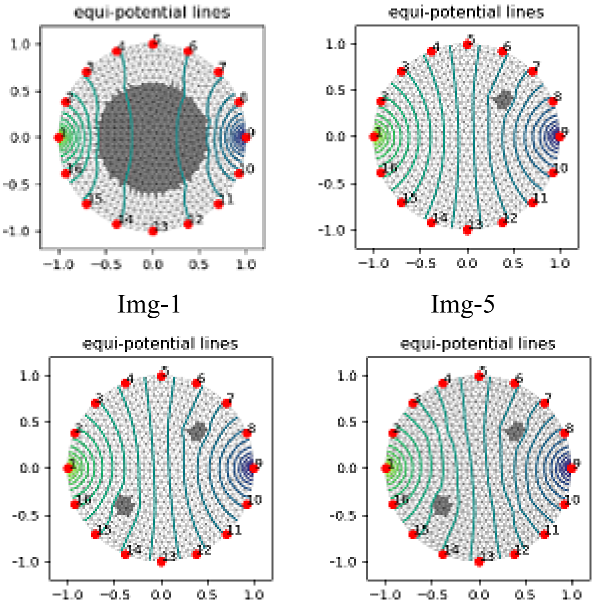

Img-1 Img-5

Img-3 Img-7

Figure 6. Equipotential lines of selected test images.

The equipotential lines represent the spatial distribution of electrical potential across the domain, providing crucial insights into how current flows through areas of varying conductivity. As depicted in the figure, the shapes of these lines are significantly influenced by the presence of inclusions with different sizes and conductivity values. For instance, inclusions with higher conductivity create denser equipotential lines, indicating a more substantial current flow through those regions. In contrast, low-conductivity inclusions result in more widely spaced lines, reflecting a reduction in current flow.

Moreover, the geometry of the inclusions affects the overall shape and orientation of the equipotential lines, demonstrating how the surrounding medium interacts with the introduced variations in conductivity. By analyzing the equipotential line distribution, one can infer the location and extent of the inclusions and their impact on the overall electrical behavior of the phantom. The findings illustrated in Figure 6 highlight the intricate relationship between the conductive properties of materials and the resultant electrical field distribution, underscoring the importance of accurate modeling in EIT applications.

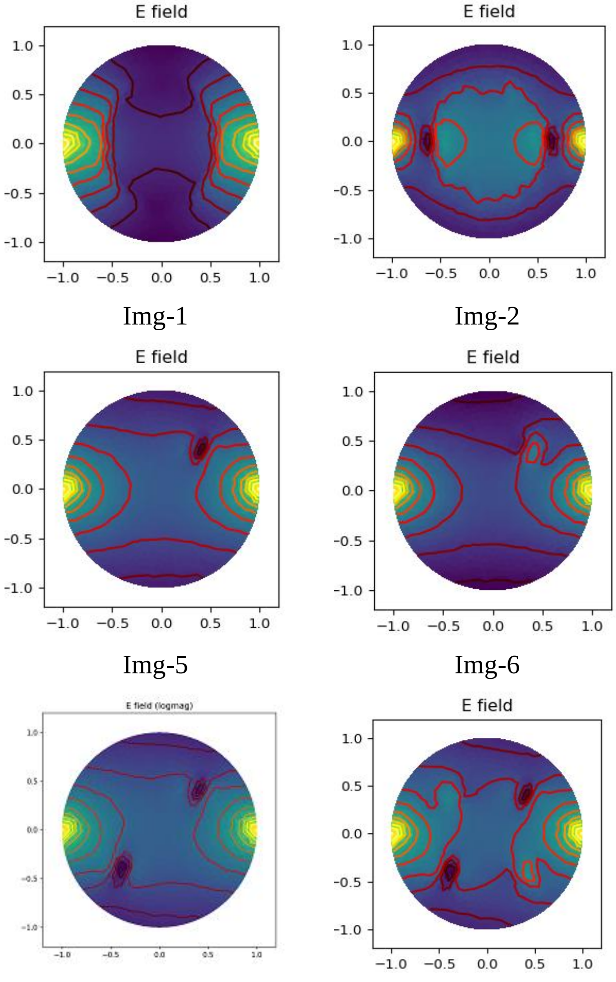

Img-1 Img-2

Img-5 Img-6

Img-5 Img-7

Figure 7. Electric fields of selected test images.

Figure 7 illustrates the calculated electric field distribution (E) for six of the test images analyzed in this study. Each image provides a detailed visualization of how the electric field varies across the domain, revealing the complex interactions between the injected currents and the conductivity distributions within the phantom.

By examining the electric field distributions depicted in Figure 7, one can infer important characteristics about the geometry and electrical properties of the inclusions. The electric field patterns provide insights into how effectively the current flows through different regions, which is vital for interpreting the results of the image reconstruction algorithms. The variations in electric field strength and direction reflect the conductive properties of the materials involved and highlight the inclusions' influence on the phantom's overall electrical behavior.

Figure 8 compares reconstructed images derived from two distinct test cases. The upper portion of the figure showcases the reconstruction of Img-1, using both the delta conductivity method and the JAC method. In contrast, the lower section of the figure displays the reconstruction results for Img-2, characterized by a significantly lower conductivity.

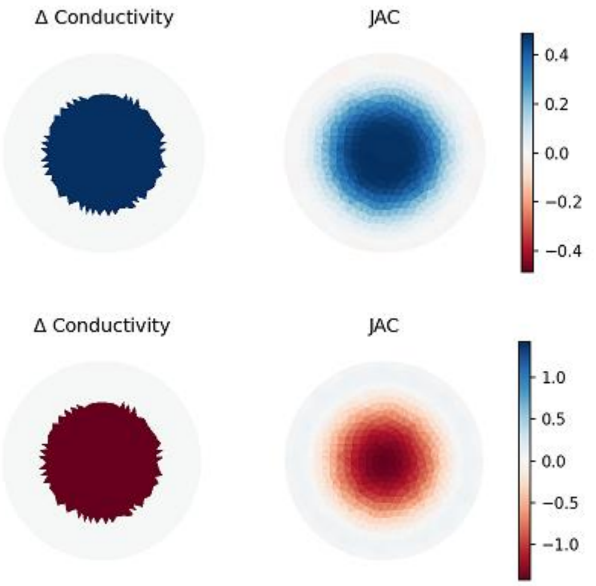

Figure 8. Reconstructed images of Img-1 and Img-2 using the delta conductivity method and JAC method.

For Img-1, the reconstructed images highlight how the methods effectively represent the high conductivity inclusion, albeit with some discrepancies in terms of the precise boundaries and the overall intensity of the reconstructed regions. Similarly, for Img-2, the low conductivity inclusion presents its own challenges, with both methods capturing the inclusion's general shape but differing in detail and accuracy.

Both upper and lower images illustrate the reconstruction methods' effectiveness in capturing the conductivity inclusions' general shape and features. However, while the visually reconstructed images appear similar, subtle differences can be observed between them. Although both aimed at accurately reconstructing the conductivity distribution, the delta conductivity method and the JAC method may yield slightly varied results due to their differing approaches to handling the forward problem and the iterative nature of the reconstruction process.

The upper section of Figure 9 displays the reconstructed images for Img-5, a test image with an upper right inclusion of high conductivity (σ = 5 S/cm) and a lower left inclusion of low conductivity (σ = 0.1 S/cm). The delta conductivity and JAC methods were applied to this configuration. The reconstructed images appear to effectively capture the contrast in conductivity, although indirect differences in boundary sharpness and intensity can be noted between the two methods.

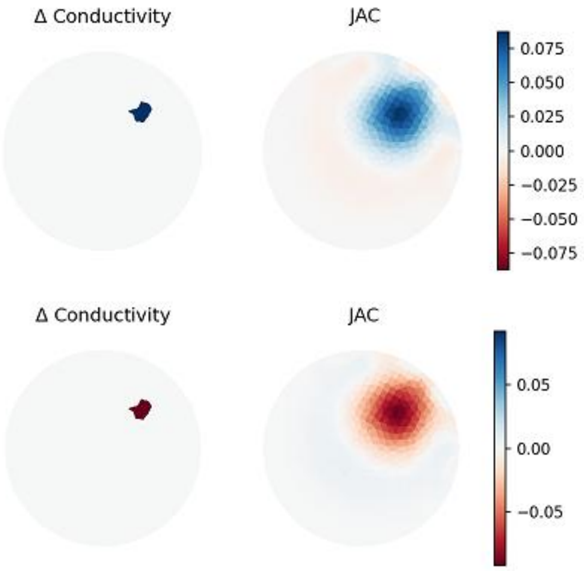

Figure 9. Reconstructed images of Img-5 and Img-6 using the delta conductivity method and JAC method.

In the lower section of Figure 9, the reconstructed images for Img-6 are shown. In this case, the configuration is similar to Img-5 but with the conductivities reversed: the upper right inclusion has low conductivity (σ = 0.1 S/cm) and the lower left inclusion has high conductivity (σ = 5 S/cm). The delta conductivity and JAC methods successfully reproduce the general structure of the inclusions, though visual discrepancies in resolution and edge definition can be observed. This highlights the inherent differences in how the two methods handle variations in conductivity, with the JAC method generally offering smoother transitions at the boundaries compared to the delta conductivity approach.

Figure 10 continues the comparison with Img-3 in the upper section. This image contains a single inclusion at the upper corner of the domain with a high conductivity of σ = 5 S/cm. The reconstructions using both methods display reasonable accuracy in capturing the location and size of the inclusion. However, closer inspection reveals that the JAC method tends to provide a slightly clearer delineation of the inclusion's boundary compared to the delta conductivity method, which shows some blurring in the transition regions.

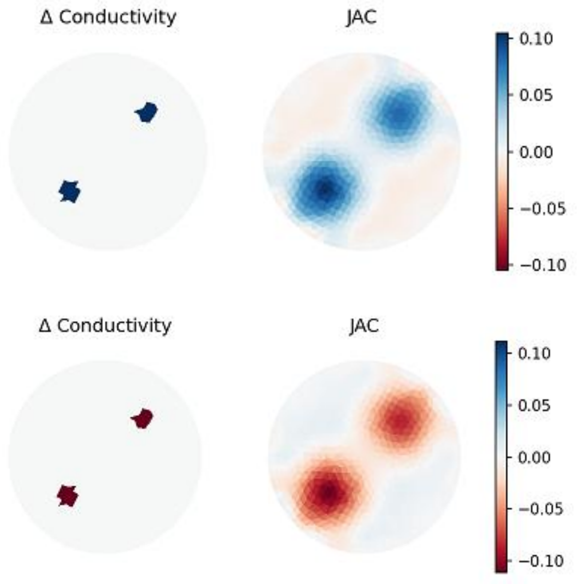

Figure 10. Reconstructed images of Img-3 and Img-4 using the delta conductivity method and JAC method.

The lower section of Figure 10 presents the results for Img-4, which has a similar configuration to Img-3 but with the inclusion assigned a lower conductivity of σ = 0.1 S/cm. Both reconstruction methods handle the low-conductivity inclusion reasonably well, but again, the JAC method seems to offer better contrast and sharper details in comparison to the delta conductivity approach. This suggests that the JAC method might be more adept at resolving fine features in regions of low conductivity.

Figure 11 focuses on Img-7, a more complex test image featuring four inclusions distributed across the domain. The upper right and lower left inclusions have high conductivities (σ = 5 S/cm), while the upper left and lower right inclusions are characterized by low conductivities (σ = 0.1 S/cm). The reconstructed images using the delta conductivity and JAC methods capture the inclusions' overall structure and positioning. However, the JAC method again demonstrates a slight advantage in reconstructing finer details and providing a more consistent representation of the inclusions' boundaries.

For Img-7, the delta conductivity method shows some smearing and less precise boundary definition, particularly in the regions with high conductivity. The JAC method, by contrast, delivers more distinct edges and a smoother representation of the conductivity gradient between inclusions, making it appear more refined and accurate.

Figure 11. Reconstructed image of Img-7 using the delta conductivity method and JAC method.

These figures provide a detailed visual comparison between the delta conductivity method and the JAC method across a range of test images with different conductivity distributions. While both methods can reconstruct the inclusions with reasonable accuracy, the JAC method consistently exhibits superior performance in terms of boundary sharpness, contrast, and overall clarity. This suggests that the JAC method is better suited for applications where precise delineation of conductive regions is critical, while the delta conductivity method may suffice for simpler reconstructions where high precision is less crucial.

Table 1 presents the performance metrics used to evaluate the quality of reconstructed images from Img-1 to Img-7 in terms of PSNR, MSE, and MSSIM. These metrics provide a quantitative assessment of how closely the reconstructed images match the theoretical test images, offering insights into both the accuracy and quality of the reconstruction process.

Table 1. Images PSNR, MSE and MSSIM values.

Image	PSNR dB	MSE	MSSIM
Img-1	35.13	19.68	0.91856
Img-2	35.76	17.26	0.87509
Img-3	36.76	13.96	0.96722
Img-4	37.96	10.65	0.96292
Img-5	34.94	21.68	0.94399
Img-6	35.55	18.49	0.93712
Img-7	33.84	26.93	0.88499
Average	35.71	18.38	0.92713

In Table 1, the PSNR values range from 33.84 dB (Img-7) to 37.96 dB (Img-4). On average, the PSNR is 35.71 dB, suggesting that most reconstructed images exhibit high reliability with respect to the original test images. However, Img-7 demonstrates a slightly lower PSNR, indicating more noise or error in that particular reconstruction.

In Table 1, the MSE values range from 10.65 (Img-4) to 26.93 (Img-7), with an average of 18.38 across all images. Img-4, which has the lowest MSE (10.65), reflects the highest accuracy, while Img-7, with the highest MSE (26.93), shows the least accurate reconstruction. This is consistent with Img-7's lower PSNR score, further supporting that this image has more deviations from the original.

In Table 1, MSSIM values are generally high, ranging from 0.87509 (Img-2) to 0.96722 (Img-3), with an average MSSIM of 0.93. The high MSSIM values across the board suggest that the reconstruction algorithms effectively preserve the original images' structural content, even if minor errors exist in pixel intensity (as indicated by PSNR and MSE). Img-3, with the highest MSSIM of 0.96722, demonstrates the best structural similarity, while Img-2, with the lowest MSSIM (0.87509), exhibits slightly reduced structural accuracy.

Figure 12 provides a comparative analysis of image quality metrics for the reconstructed test images, showcasing both PSNR and SSIM values.

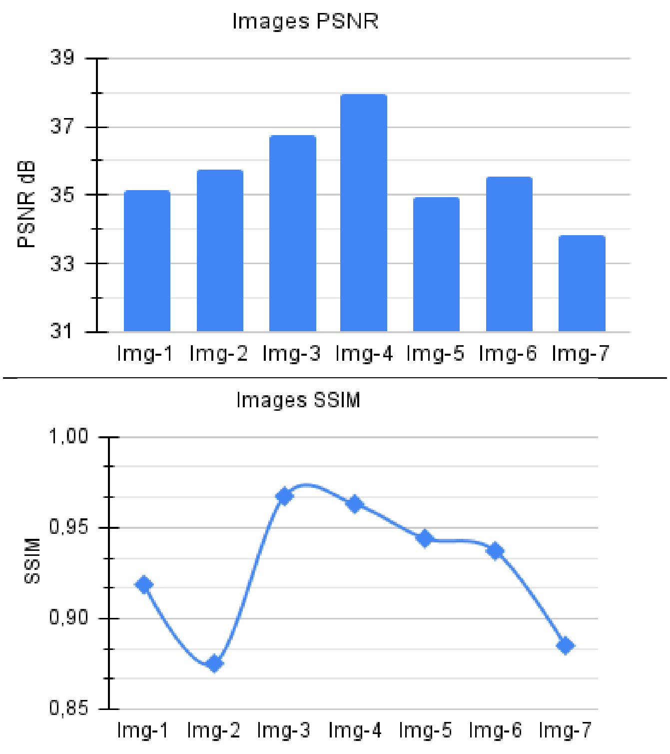

Figure 12. Test images PSNR and MSSIM graph.

The upper part of Figure 12 presents a bar diagram illustrating the PSNR values for each test image, from Img-1 to Img-7. This diagram highlights the variations in image reconstruction quality across different conductivity distributions, with higher PSNR values indicating better reconstruction fidelity relative to the original test images. The lower part of Figure 12 displays the corresponding MSSIM values for the same set of test images. MSSIM, which assesses the mean structural similarity between the reconstructed and original images, provides insight into the perceptual quality of the reconstructions. Higher MSSIM values signify closer texture, contrast, and luminance similarity between the reconstructed and original images.

Earlier studies in the field, primarily concentrated on traditional methods like linearized techniques and Gauss-Newton-based inversion algorithms, which relied on prior information and regularization to stabilize the reconstruction process [6]. These methods typically yielded satisfactory results for relatively simple phantoms with low complexity. However, as the complexity of the test images increased the performance of these methods began to degrade. Such degradation was particularly noticeable when the inclusion size and conductivity contrasts were small, as the methods struggled to accurately capture finer details in the conductivity distribution [14].

More recent studies explored the use of advanced regularization methods. Including non-linear models, complex geometries, and multi-frequency data improved accuracy in reconstructing phantoms with more complex structures and smaller contrasts. However, some challenges remained, particularly in reconstructing images with intricate textures or multiple inclusions, where the reconstruction could still be affected by noise or limited resolution [1, 30].

Machine learning (ML) models have demonstrated a significant advantage over traditional solver algorithms in EIT, offering new opportunities for its application in industrial processes [2]. In a systematic study, Martı Aller and David Mera et. al, compared several ML approaches, including Artificial Neural Networks (ANN), Elastic Net (EN), Random Forest (RF), K-Nearest Neighbors (KNN), AdaBoost (AB), and Gradient Boosting (GB), as inverse solvers. These models were assessed from both quantitative and qualitative perspectives. While all models provided acceptable results, the Gradient Boosting (GB) model, which leverages decision tree learners, exhibited the best performance, achieving superior metrics with minimal statistical dispersion. Additionally, Lin Yang and Zhe Li et al. proposed using XGBoost, an advanced boosting method, which demonstrated the best overall performance for balanced EIT image reconstruction. XGBoost also supports parallelization, improving computational efficiency while reducing the risk of overfitting, positioning it as a promising ML method for predictive applications, such as early forecasting of high-flow nasal cannula (HFNC) outcomes [31]. These studies underscore the growing role of machine learning in enhancing electroencephalography's capabilities and expanding its potential applications [34].

The delta conductivity method demonstrated faster convergence, especially when the initial guess was close to the true conductivity distribution. However, it was more sensitive to noise, requiring higher regularization parameters for stable results. In contrast, the Jacobian-based method provided more stable reconstructions but required more iterations and was computationally more intensive.

5. Discussion

The study systematically evaluates the performance of two widely used image reconstruction algorithms in EIT, the delta conductivity update method and the JAC-based method. The evaluation underscores the importance of regularization in stabilizing the inherently ill-posed EIT inverse problem. Both methods benefited from the inclusion of regularization terms, which mitigated the effects of noise in the measured voltages and prevented overfitting. Nonetheless, the choice of regularization parameter remains a critical factor influencing reconstruction quality, necessitating further exploration to optimize its selection for different imaging scenarios.

Another notable observation is the sensitivity of reconstruction accuracy to the initial guess of conductivity distribution. Both algorithms exhibited faster convergence and higher accuracy when the initial guess was closer to the true conductivity distribution, highlighting the potential advantage of incorporating prior knowledge or adaptive initialization strategies in EIT image reconstruction workflows.

Future work could explore hybrid approaches combining the strengths of both methods, advanced regularization techniques, and machine learning-based frameworks to enhance reconstruction accuracy and efficiency further.

6. Conclusions

In this study, we quantitatively assessed two widely used image reconstruction algorithms: the delta conductivity update method and JAC-based method within EIT. By evaluating seven test images with varying levels of complexity, we compared the performance of these algorithms using key image quality metrics.

The results demonstrated that both methods effectively reconstruct the conductivity distribution within the phantom, but each has distinct strengths. The JAC-based method showed improved performance, especially in scenarios involving complex geometries and multiple inclusions, owing to its ability to handle intricate conductivity variations. In contrast, the delta conductivity method provided reasonably accurate reconstructions for more straightforward images with lower computational overhead. On average, the reconstructed images achieved PSNR and MSSIM values of 35.71 dB and 0.93, respectively, indicating good overall reconstruction quality across the test images. However, as image complexity increased, the reconstruction accuracy, particularly with the delta conductivity method, decreased, underscoring the challenge of reconstructing highly detailed or complex phantoms in EIT.

Our findings highlight the need to select an appropriate reconstruction method based on the specific imaging scenario. Future work could explore the integration of more advanced regularization techniques or hybrid methods that combine the strengths of both algorithms.

Declaration of Ethical Standards

The author of this article declares that the materials and methods used in this study do not require ethical committee permission and/or legal-special permission.

Conflict of Interest

The author declares that he has no known competing financial interests or personal relationships that could have appeared to influence the work reported in this paper.

References

[1] Li, Y., Wang, N., Fan, L.F., Zhao, P.F., Li, J. H., Huang, L., Wang, Z.Y., 2023. Robust electrical impedance tomography for biological application: a mini review. Heliyon, **9**(4).

[2] Aller, M., Mera, D., Cotos, J. M., & Villaroya, S., 2023. Study and comparison of different Machine Learning-based approaches to solve the inverse problem in Electrical Impedance Tomographies. Neural Computing and Applications, **35**(7), 5465-5477.

[3] Manisalı, H., 2020. Elektrik Empedans Tomografide Eliptik Yapılardaki İletkenlik Dağılımları Geriçatım Probleminin Yapay Sinir Ağları ile İncelenmesi. Yüksek Lisans Tezi, Hacettepe Üniversitesi.

[4] Oz, I., 2024. New Approaches in Engineering Sciences, Finite Element-Based Imaging for Electrical Impedance Tomography. Platanus Publishing, Turkey

[5] Ziegler, S., Santos, T., & Mueller, J. L. 2024. Regularized full waveform inversion for low frequency ultrasound tomography with a structural

similarity EIT prior. Inverse Problems and Imaging. **18**(1), 86-103.

[6] Ozkan, I., 1995. Elektriksel empedans tomografisi. Doktora tezi, Fen Bilimleri Enstitüsü Osmangazi Üniversitesi.

[7] Oz, I., 1996. Empedans tomografisinde sonlu elemanlar yönte-mi ile görüntü oluşturulması. Yüksek Lisans Tezi, Fen Bilimleri Enstitüsü, Dumlupınar Üniversitesi.

[8] Dimas, C., & Sotiriadis, P. P., 2018. Electrical impedance tomography image reconstruction for adjacent and opposite strategy using FEMM and EIDORS simulation models. IEEE 7th International Conference on Modern Circuits and Systems Technologies (MOCAST) (pp. 1-4).

[9] Hamilton, S. J., Lionheart, W. R. B., & Adler, A., 2019. Comparing D-bar and common regularization-based methods for electrical impedance tomography. Physiological measurement, **40**(4), 044004.

[10] Cen, S., Jin, B., Shin, K., & Zhou, Z., 2023. Electrical impedance tomography with deep Calderón method. Journal of Computational Physics, **493**, 112427.

[11] Brinckerhoff, M., 2018. Comparison of electrical impedance tomography reconstruction algorithms with EIDORS reconstruction software. Master's thesis, Clemson University.

[12] Mosquera, V., Gonzalez, C., & Ortega, E., 2019. Eidors-matlab interface for forward problem solving of electrical impedance tomography.

[13] Hauptmann, A., Kolehmainen, V., Mach, N. M., Savolainen, T., Seppänen, A., & Siltanen, S., 2017. Open 2D electrical impedance tomography data archive. arXiv preprint arXiv:1704.01178.

[14] Hakula, H., Hyvönen, N., & Tuominen, T., 2012. On the hp-adaptive solution of complete electrode model forward problems of electrical impedance tomography. Journal of computational and applied mathematics, **236**(18), 4645-4659.

[15] Sarode, V., Chimurkar, P. M., & Cheeran, A. N., 2012. Electrical impedance tomography using EIDORS in a closed phantom. International Journal of Computer Applications, **48**(19), 975-888.

[16] Zong, Z., Wang, Y., He, S., Zhu, Y. J., & Wei, Z., 2023. A compressive learning-based scheme for nonlinear reconstructions in electrical impedance tomography. IEEE Transactions on Instrumentation and Measurement.

[17] Sarode, V., Patkar, S., & Cheeran, A. N., 2013. Comparison of 2-D algorithms in ElT based image reconstruction. International Journal of Computer Applications, **69**(8), 6-11.

[18] Yang, Y., Wu, H., & Jia, J. 2017. Image reconstruction for electrical impedance tomography using enhanced adaptive group sparsity with total variation. IEEE Sensors Journal, **17**(17), 5589-5598.

[19] Pennati, F., Angelucci, A., Morelli, L., Bardini, S., Barzanti, E., Cavallini, F., & Aliverti, A., 2023. Electrical impedance tomography: From the traditional design to the novel frontier of wearables. Sensors, **23**(3), 1182.

[20] Wang, Z., Zhang, X., Fu, R., Wang, D., Chen, X., & Wang, H., 2023. Electrical impedance tomography image reconstruction with attention-based deep convolutional neural network. IEEE Transactions on Instrumentation and Measurement, **72**, 1-18.

[21] Salkım, E., & Abut, T., 2024. Human Head Transcranial Magnetic Stimulation Using Finite Element Method. Kocaeli Journal of Science and Engineering, **7**(1), 62-70.

[22] Kilic, B., 2019. Impedance image reconstruction with artificial neural network in electrical impedance tomography. European Journal of Technique (EJT), **9**(2), 137-144.

[23] Dong, Q., Zhang, Y., He, Q., Xu, C., & Pan, X., 2023. Image reconstruction method for electrical impedance tomography based on RBF and attention mechanism. Computers and Electrical Engineering., **110**, 108826.

[24] Oz, I., 2024. Comparative Analysis of Wavelet Families in Image Compression, Featuring the Proposed New Wavelet. Turkish Journal of Science and Technology, **19**(1), 279-294. https://doi.org/10.55525/tjst.1428424

[25] Oz, I. 2006. İki Boyutlu Ayrık Dalgacık Dönüşüm Filtreleri Kullanarak Sabit ve Hareketli Görüntü Sıkıştırma. Doktora Tezi, Sakarya Üniversitesi, Sakarya, Turkey.

[26] Oz, I, Oz, C, Yumusak N., 2001. Image compression using 2-D multiple-level discrete wavelet transform (DWT). Eleco 2001 International Conference on Electrical and Electronics Engineering, Turkey.

[27] Burukanli, M., & Yumuşak, N., 2024. TfrAdmCov: a robust transformer encoder based model with Adam optimizer algorithm for COVID-19 mutation prediction. Connection Science, **36**(1), 2365334.

[28] Yılmaz, G. N., & Akar, G. B., 2022. SSIM Modelin Geliştirilmesine Dayanan Bir 3B Video Kalite Değerlendirme Metriği. Türkiye Bilişim Vakfı Bilgisayar Bilimleri ve Mühendisliği Dergisi, **15**(1), 1-5.

[29] Sun, J., Zhu, Q., Fang, H., Wang, J., Zhou, W., Liu, Z., & Yang, Y., 2024. Multi-Modal EIT Image Reconstruction Using Deep Similarity Prior. IEEE International Instrumentation and Measurement Technology Conference (I2MTC) (pp. 1-6). IEEE.

[30] Chen, J., Wang, S., Wang, K., Abiri, P., Huang, Z. Y., Yin, J., ... & Hsiai, T. K., 2024. Machine learning-directed electrical impedance tomography to predict metabolically vulnerable plaques. Bioengineering & translational medicine, **9**(1), e10616.

[31] Yang, L., Li, Z., Dai, M., Fu, F., Möller, K., Gao, Y., & Zhao, Z., 2023. Optimal machine learning methods for prediction of high-flow nasal cannula outcomes using image features from electrical impedance tomography. Computer Methods and Programs in Biomedicine, **238**, 107613.

[32] Salkım, E., 2023. Transcutaneous Nerve Stimulation Current Thresholds Based on Nerve Bending Angle and Nerve Termination Point. Kocaeli Journal of Science and Engineering, **6**(2), 162-171.

[33] Liu, Benyuan, et al. "pyEIT: A python based framework for Electrical Impedance Tomography." SoftwareX **7** (2018), 304-308.

[34] Melek, N., 2024. The Importance of Rhythm Activity in Epilepsy EEG Signal Classification (An Educational Article). Sakarya University Journal of Computer and Information Sciences, **7**(2), 138-155.

[35] Oz, I., 2024. Compression Methods For Satellite Images Using Wavelet Transform And Performance Evaluation. International Journal of Innovative Engineering Applications, 8(2), 72-81. doi:10.46460/ijiea.1440970